A Sliding Mode Control Law for Mobile Robots based on Epipolar Visual Servoing from Three Views

H. M. Becerra, G. Lopez-Nicolas and C. Sagues[‡]

February 15, 2011

Abstract

Driving mobile robots to precise locations is of recognized interest, and using vision sensors in this context supplies many advantages. We propose a novel control law based on sliding mode theory in order to drive mobile robots to a target location, which is specified by a reference image previously acquired. The control scheme exploits the piecewise epipolar geometry of three views on the basis of image-based visual servoing, in such a way that no 3D scene information is required. The contribution of the paper is a new control law that achieves convergence to the target with no auxiliary images and without changing to any approach other than epipolar-based control. Additionally, the use of sliding mode control deals with singularities allowing the robot to move directly toward the target and also avoiding the need of a precise camera calibration. The effectiveness of our approach is tested with simulations and real-world experiments.

1 INTRODUCTION

There is an increasing interest of the robotics research community on topics related to service robots, which usually are wheeled platforms. This paper presents a control scheme to drive a wheeled mobile robot to a desired location that is specified by a target image previously acquired, i.e. the teach-by-showing strategy. The feasibility of visual control in robotic applications has been well studied previously [1]. Particularly, vision is a useful tool for enhancing the navigation capability of mobile robots [2]. An intuitive application of the proposed approach is robot navigation using a visual memory to follow a sequence of target images. This may be meaningful in the framework of inspection robots, which are required to look at some specific views, or in autonomous personal transportation vehicles.

The proposed control scheme is classified as an image-based scheme. In this type of approach the image data is used directly in the control loop, unlike the position-based schemes, where an estimate of pose parameters is needed. Different image-based approaches have been used for control of mobile robots, from the classical Jacobian-based schemes that are based on a non-exact inversion of a rectangular interaction matrix [3], [4], to schemes that exploit a geometric constraint that relates image features [5], [6], [7], [8]. In general, classical Jacobian-based schemes are sensitive to image noise and depend on the estimation of the structure of the scene (depth) [9]. Additionally, they exhibit potential problems of stability [10] and only local stability can be theoretically demonstrated. Although lines have been proposed to achieve robustness to image noise [11], the use of geometric constraints is a good alternative to improve robustness against image noise and to ensure correct correspondences between image features [12].

Particularly, the epipolar geometry has been applied for control of robot manipulators [13], [14]. The drawbacks of this geometry are the ill-conditioning for planar scenes, the degeneracy with short baseline and singularity problems for system control. In related works about visual servoing of mobile robots, the first issue has been solved by using a generic scene and the second has been tackled by commuting to a feature-based strategy [7] or homography-based control [15]. The singularity problems in epipolar-based control appear when the interaction matrix between the robot velocities and the rate of change of the epipoles becomes singular for some state of the robot. In fact, unbounded velocities eventually appear because the singularity is always reached when the robot moves directly toward the target. The approach in [7] takes into account the nonholonomic nature of a wheeled robot by driving one dimension of the epipoles to zero in a smooth way. However, in order to avoid the singularity, the motion strategy steers the robot away from the target while the lateral error is corrected, and after that, the robot moves backward to the target position. A more intuitive way to drive the robot directly toward the target has been addressed in [16] but the singularity is not treated. An approach

*This work was supported by project DPI 2009-08126 and grants of Banco Santander-Univ. Zaragoza and Conacyt-México.

†H.M. Becerra, G. Lopez-Nicolas and C. Sagues are with Instituto de Investigación en Ingeniería de Aragón, Universidad de Zaragoza C/ María de Luna 1, E-50018 Zaragoza, Spain (email: hector.becerra@unizar.es, gonlopez@unizar.es, csagues@unizar.es).

that exploits the decomposition of the epipolar geometry for visual path following with mobile robots is presented in [17].

An important concern in visual servoing schemes is the uncertainty in calibration parameters. Some works have tackled the uncalibrated visual servoing problem for robot manipulators, for instance the Jacobian-based approach [18], which keeps the potential problems of such schemes. The proposal in [19] avoids the dependence on depth information but requires the robot dynamics and additional feedback of position and velocity.

This paper focuses on the development of a sliding mode control (SMC) law that exploits the epipolar geometries among three views. This is an extension of [20], which introduces a robust two-view-based control law that is able to correct orientation and lateral error but not depth. In the work herein, we extend the epipolar geometry to three images taken in pairs to correct also depth only from the epipolar constraint. The trifocal tensor has been recently used for visual servoing emphasizing the benefits of three-view based schemes [8]. The epipolar geometry is an approach for general scenes that provides a filtering of the visual measurements. Our scheme ensures stability of the closed loop by working with a squared control system and does not need any geometric decomposition or additional parameter estimation to achieve pose regulation. The use of a third image allows us to unify the control scheme in only one type of image-based controller for the whole task.

In summary, the main contributions of this paper with respect to previous epipolar-based approaches are that the proposed control law corrects position and orientation by keeping full control during the whole task using only epipolar feedback. The control law copes with singularities induced by the epipolar geometry also improving the robot behavior by performing a direct motion toward the target. Besides, the use of the SMC technique allows robust global stabilization of the task function (including image noise) when dealing with the weak calibration problem (i.e., with no specific calibration).

The paper is organized as follows. Section II specifies the mathematical modeling that is used for the visual sensor, the mobile robot and the epipolar geometry. Section III details the design procedure for the SMC law. The stability and robustness analysis is presented in Section IV. Section V shows the performance of the control scheme with simulations and real-world experiments.

2 MATHEMATICAL MODELING

2.1 Visual Sensing and Robot Kinematics

Consider the geometry of a finite projective camera to be modeled by perspective projection, whose internal calibration matrix is

$$\mathbf{K} = \begin{bmatrix} \alpha_x & s & x_0 \\ 0 & \alpha_y & y_0 \\ 0 & 0 & 1 \end{bmatrix} \tag{1}$$

where $\alpha_x = fm_x$ and $\alpha_y = fm_y$ are the focal length of the camera in terms of pixel dimensions in the x and y directions respectively, with m_x and m_y the number of pixels per unit distance, and f the focal length in distance units. s is the skew parameter and (x_0, y_0) are the coordinates of the principal point in pixels. We assume that the principal point is in the center of the image ($x_0 = 0$, $y_0 = 0$) and there is no skew ($s = 0$). An image is denoted by $I(\mathbf{K}, \mathbf{C})$, where $\mathbf{C}$ represents the extrinsic parameters.

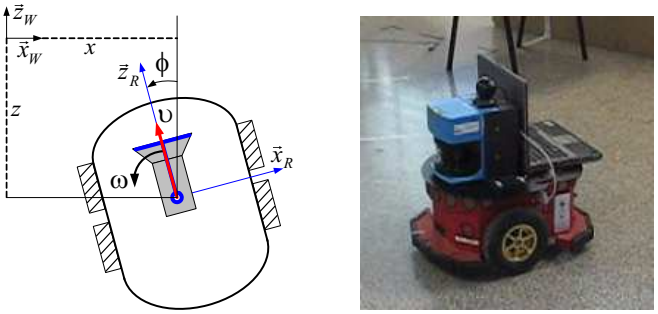

(a) (b)

Figure 1: Robotic system. (a) Frame definitions with $\vec{x}_W$, $\vec{z}_W$ the axis of the world frame and $\vec{x}_R$, $\vec{z}_R$ the corresponding for the robot frame. (b) Experimental platform.

The system to be controlled is a differential-drive robot, whose kinematic model can be expressed in accordance with the frame defined in Fig. 1(a) as follows

$$\begin{bmatrix} \dot{x} \\ \dot{z} \\ \dot{\phi} \end{bmatrix} = \begin{bmatrix} -\sin\phi & 0 \\ \cos\phi & 0 \\ 0 & 1 \end{bmatrix} \begin{bmatrix} v \\ \omega \end{bmatrix} \tag{2}$$

where $\mathbf{x} = (x, z, \phi)^T$ represents the state of the robot, being $x(t)$ and $z(t)$ the robot position in the plane and $\phi(t)$ the robot orientation. Additionally, $v(t)$ and $\omega(t)$ are the translational and rotational input velocities. This model represents the kinematic motion of the experimental platform of Fig. 1(b). Notice that the camera is placed in such a way that the robot and camera frames are aligned and their origins coincide with the vertical axis of rotation.

2.2 Pairwise Epipolar Geometry of Three Views

The epipolar geometry describes the intrinsic geometry between two views and only depends on the relative location between cameras and their internal parameters. The fundamental matrix $\mathbf{F} \in \mathbb{R}^{3\times3}$ is the algebraic representation of this geometry and can be computed by solving a linear system of equations using the 8-point algorithm [12]. The epipoles can be estimated as the null vectors of $\mathbf{F}$ and $\mathbf{F}^T$.

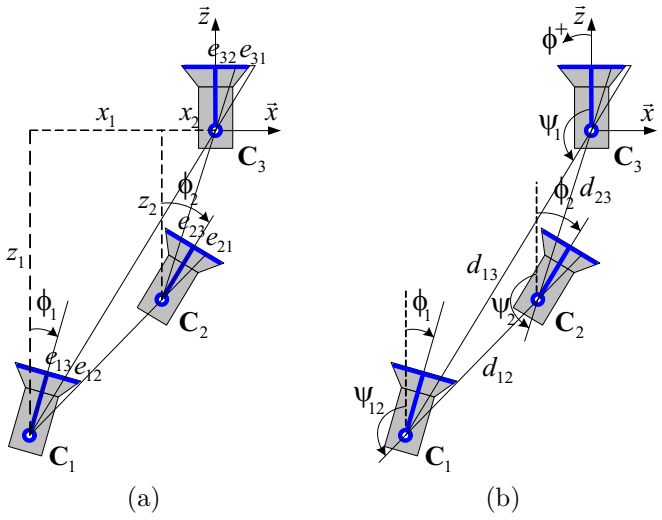

Figure 2: Pairwise epipolar geometry of three views. (a) Cartesian locations defining the epipoles among three views. (c) Polar coordinates.

According to Fig. 2(a) and using the general case for a pair of views [16], we can find the six epipoles among three views. Let $\mathbf{C}_1 = (x_1, z_1, \phi_1)$ and $\mathbf{C}_2 = (x_2, z_2, \phi_2)$ be two camera locations with respect to a global reference in $\mathbf{C}_3 = (0, 0, 0)$, associated to the location of the target image. In our camera-robot configuration the x-coordinate of the epipoles can be written as a function of the robot state and the parameter α_x. The double subscript refers to the related images, for instance, e_{13} is the epipole in image one, as computed with respect to image three.

$$e_{13} = \alpha_x \frac{x_1\cos\phi_1 + z_1\sin\phi_1}{z_1\cos\phi_1 - x_1\sin\phi_1}, \tag{3}$$

$$e_{31} = \alpha_x \frac{x_1}{z_1},$$

$$e_{23} = \alpha_x \frac{x_2\cos\phi_2 + z_2\sin\phi_2}{z_2\cos\phi_2 - x_2\sin\phi_2}, \tag{4}$$

$$e_{32} = \alpha_x \frac{x_2}{z_2},$$

$$e_{12} = \alpha_x \frac{(x_1 - x_2)\cos\phi_1 + (z_1 - z_2)\sin\phi_1}{(z_1 - z_2)\cos\phi_1 - (x_1 - x_2)\sin\phi_1}, \tag{5}$$

$$e_{21} = \alpha_x \frac{(x_1 - x_2)\cos\phi_2 + (z_1 - z_2)\sin\phi_2}{(z_1 - z_2)\cos\phi_2 - (x_1 - x_2)\sin\phi_2}.$$

The Cartesian coordinates for the camera location $\mathbf{C}_2$ can be expressed as a function of the polar coordinates d_{23} and ψ_2 (Fig. 2(b)) using

$$x_2 = -d_{23}\sin\psi_2, \quad z_2 = d_{23}\cos\psi_2, \tag{6}$$

with $\psi_2 = -\arctan(e_{32}/\alpha_x)$, $\phi_2 - \psi_2 = \arctan(e_{23}/\alpha_x)$ and $d_{23}^2 = x_2^2 + z_2^2$. Similarly, the relative Cartesian coordinates between $\mathbf{C}_1$ and $\mathbf{C}_2$ can be expressed from the polar coordinates d_{12} and ψ_{12} as follows

$$(x_1 - x_2) = -d_{12}\sin\psi_{12}, \quad (z_1 - z_2) = d_{12}\cos\psi_{12}, \tag{7}$$

with $\psi_{12} = \phi_2 - \arctan(e_{21}/\alpha_x) = \phi_1 - \arctan(e_{12}/\alpha_x)$ and $d_{12}^2 = (x_1 - x_2)^2 + (z_1 - z_2)^2$.

3 CONTROL LAW DESIGN

We propose to correct the robot pose by exploiting the epipolar geometries among three views. This is done on the basis of a squared control system, where global stability can be ensured in contrast to rectangular Jacobian-based approaches [9]. Henceforth, let $\mathbf{C}_1$ be the initial camera location, $\mathbf{C}_2$ the current and $\mathbf{C}_3$ the target location. The proposed control strategy is performed in two steps as follows:

- First step. Alignment with the target: orientation and lateral error are corrected. This is achieved by zeroing the epipoles relating the current image $I_2(\mathbf{K}, \mathbf{C}_2(t))$ and the target one $I_3(\mathbf{K}, \mathbf{0})$. It can be seen as a two-view approach because only requires the epipoles e_{23} and e_{32}. Initially, we have two images (Fig. 3(a)) and at the end of this step, the robot is as in Fig. 3(b).
- Second step. Depth correction: pure translation along the $z-$axis. Provided that the orientation and the lateral error are maintained in zero by the control loop, the objective of this step is to achieve $e_{12} = e_{13}$ or $e_{21} = e_{31}$. This step requires the three images to compute the constant epipoles e_{13}, e_{31} from $I_1(\mathbf{K}, \mathbf{C}_1)$, $I_3(\mathbf{K}, \mathbf{0})$ and the varying epipoles e_{12}, e_{21} from $I_1(\mathbf{K}, \mathbf{C}_1)$, $I_2(\mathbf{K}, \mathbf{C}_2(t))$.

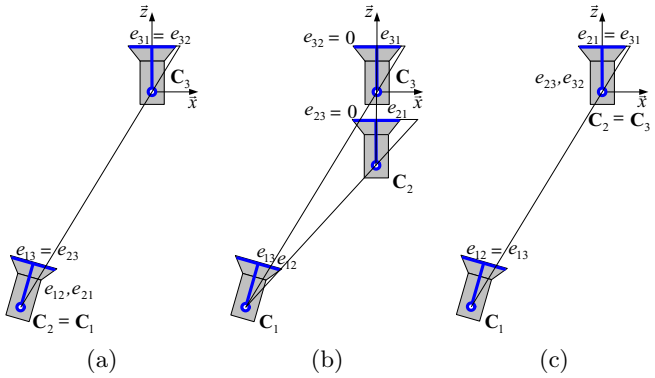

Figure 3: Control strategy from the epipoles of three views. (a) Initial configuration. (b) Intermediate configuration. (c) Final configuration.

Finally, after the first step has corrected lateral error, the epipolar geometry in the three-view configuration is $e_{12} = e_{13}$, $e_{21} = e_{31}$, which implies $I_2(\mathbf{K}, \mathbf{C}_2) = I_3(\mathbf{K}, \mathbf{0})$, and consequently $\mathbf{C}_2 = \mathbf{C}_3$ as desired (Fig. 3(c)).

We assume that the robot is initially in a general configuration, not aligned with the target pose. Otherwise, this particular configuration can be trivially detected from the epipoles and, in that case, a simple initial motion controlling the epipoles can drive the robot to a general configuration.

3.1 First Step.- Alignment with the Target

Two drawbacks of the epipolar geometry appear when a camera is being aligned to a target using two views: uncertainty in parameters and singularity problems [15]. This section describes the synthesis of a control law from two images that copes with these issues. We propose to perform a smooth direct motion toward the target position applying adequate velocities during the whole task using the same robust control scheme even in singular situations.

Let us define the outputs of the system using the x-coordinates of the epipoles for the current and target images

$$\mathbf{y} = h(\mathbf{x}) = \left[\begin{array}{cc} e_{23}, & e_{32} \end{array} \right]^T. \tag{8}$$

In addition to the singularity problems from two views, depth correction cannot be reached with only such information. The so-called *zero dynamics* is achieved in the robot system when the epipoles defined as outputs reach to zero. Zero dynamics is described by a subset of the state space which makes the output to be identically zero [21]. In the particular case of the robot system (2) with output vector (8), this set, denoted by Z^*, is the following

$$Z^* = \{\mathbf{x} \mid e_{23} \equiv 0,\ e_{32} \equiv 0\} = \left\{ [0, z_2, 0]^T,\ z_2 \in \mathbb{R} \right\}. \tag{9}$$

The zero dynamics in this control system means that, when the epipoles e_{23} and e_{32} are zero, the lateral error and the orientation of the robot are corrected, but depth may be different to zero. As mentioned previously, this is corrected in a second step. Let us define tracking error functions as $\xi_c = e_{23} - e_{23}^d$ and $\xi_t = e_{32} - e_{32}^d$, where e_{23}^d and e_{32}^d are suitable time-varying references. From the time-derivatives of these errors and using the polar coordinates (6), we obtain the following error system

$$\left[\begin{array}{c} \dot{\xi}_c \\ \dot{\xi}_t \end{array} \right] = \left[\begin{array}{cc} \frac{-\alpha_x \sin(\phi_2 - \psi_2)}{d_{23} \cos^2(\phi_2 - \psi_2)} & \frac{\alpha_x}{\cos^2(\phi_2 - \psi_2)} \\ \frac{-\alpha_x \sin(\phi_2 - \psi_2)}{d_{23} \cos^2(\psi_2)} & 0 \end{array} \right] \left[\begin{array}{c} \upsilon \\ \omega \end{array} \right] - \left[\begin{array}{c} \dot{e}_{23}^d \\ \dot{e}_{32}^d \end{array} \right]. \tag{10}$$

The system (10) has the form $\dot{\xi} = \mathbf{M} \cdot \mathbf{u} - \dot{\mathbf{e}}^d$, where $\mathbf{M}$ corresponds to the decoupling matrix, whose inverse is

$$\mathbf{M}^{-1} = \frac{1}{\alpha_x} \left[\begin{array}{cc} 0 & -\frac{d_{23} \cos^2(\psi_2)}{\sin(\phi_2 - \psi_2)} \\ \cos^2(\phi_2 - \psi_2) & -\cos^2(\psi_2) \end{array} \right], \tag{11}$$

and $\dot{\mathbf{e}}^d$ represents a feedforward control term. In order to invert the system (10), it is important to notice that $\mathbf{M}$ loses rank if $\phi_2 - \psi_2 = n\pi$ with $n \in \mathbb{Z}$, which makes the element of the first row of (11) to grow unbounded, and consequently also the translational velocity. As can be seen in the analytical expression of the inverse matrix (11), the computation of input velocities is bounded for any other situation. From the definition of the angles below (6), it can be seen that the singular condition corresponds to $e_{23} = 0$. This is a problem because it is indeed a control objective.

We faced the tracking problem as the stabilization of the error system (10), which has unknown parameters α_x and d_{23}, i.e. focal length and distance between cameras. These parameters are estimated as the constants α_{x_e} and d_{23_e}, and introduced to the estimated decoupling matrix $\mathbf{M}_e(\phi_2, \psi_2)$.

We propose a robust control law based on SMC [22]. This control technique is chosen to tackle two issues: *i*) The sensitivity to uncertainty in parameters of a control system based on input-output linearization, which degenerates the performance of the tracking, see for example [16]. *ii*) The need to maintain control during the entire navigation even when the singularity occurs.

3.1.1 Decoupling-based Control Law

Firstly, let us define the following sliding surfaces

$$\mathbf{s} = \left[\begin{array}{c} s_c \\ s_t \end{array} \right] = \left[\begin{array}{c} \xi_c \\ \xi_t \end{array} \right] = \left[\begin{array}{c} e_{23} - e_{23}^d \\ e_{32} - e_{32}^d \end{array} \right] = \mathbf{0}. \tag{12}$$

Thus, the tracking problem is solved if there exist switched feedback gains according to an stability analysis that make the state to evolve on $\mathbf{s} = \mathbf{0}$. The following SMC law, consisting of a so-called equivalent control (feedforward term) and a two-dimensional vector of switched feedback gains, ensures global stabilization of the system (10)

$$\mathbf{u}_{sm} = \mathbf{M}_e^{-1}(\phi_2, \psi_2) \left(\begin{array}{c} \dot{e}_{23}^d - \kappa_c sign(s_c) \\ \dot{e}_{32}^d - \kappa_t sign(s_t) \end{array} \right), \tag{13}$$

being $\kappa_c > 0$ and $\kappa_t > 0$ control gains. The action of switched feedback gains in the error dynamics is to keep the state trajectory on the sliding surface (12). These gains add or subtract accordingly, in order to force the state trajectory to head always toward the surface [22]. Although (13) can achieve global stabilization of (10), it may need high gains that could cause a non-smooth behavior in the robot state, which is not valid in real situations. So, we add a pole placement term in the control law to alleviate this problem

$$\mathbf{u}_{pp} = \mathbf{M}_e^{-1}(\phi_2, \psi_2) \left[\begin{array}{cc} -\lambda_c & 0 \\ 0 & -\lambda_t \end{array} \right] \left[\begin{array}{c} s_c \\ s_t \end{array} \right], \tag{14}$$

being $\lambda_c > 0$ and $\lambda_t > 0$ control gains. Finally, the complete SMC law ($\mathbf{u} = \mathbf{u}_{db}$) that achieves robust global stabilization of the system (10) is as follows

$$\mathbf{u}_{db} = \mathbf{u}_{sm} + \mathbf{u}_{pp}. \tag{15}$$

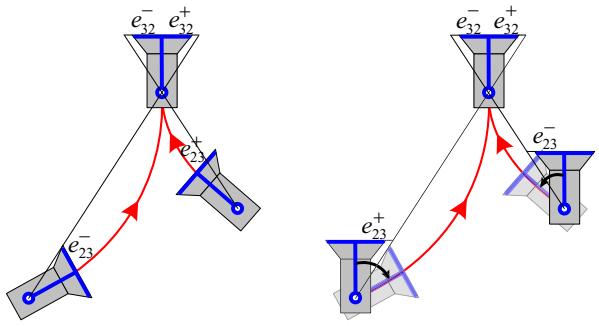

(a) (b)

Figure 4: Initial configurations requiring different motion strategy through adequate desired trajectories of the epipoles. (a) $sign\,(e_{23}) \neq sign\,(e_{32})$ - direct motion toward the target. (b) $sign\,(e_{23}) = sign\,(e_{32})$ - rotation to reach the same condition as in (a).

3.1.2 Bounded Control Law

The control law (15) utilizes the decoupling matrix that presents a singularity problem when the camera axis of the robot is aligned with the baseline, which generates unbounded translational velocity. In order to pass through the singularity, the control law commutes to a direct sliding mode controller when $|\phi_2 - \psi_2|$ is below a threshold T_h. This kind of controller has been studied for output tracking through singularities [23]. We propose the following direct sliding mode controller

$$\mathbf{u}_b = \begin{bmatrix} \upsilon_b \\ \omega_b \end{bmatrix} = \begin{bmatrix} -k_\upsilon sign\,(s_t\ b\,(\phi_2, \psi_2)) \\ -k_\omega sign(s_c) \end{bmatrix} \tag{16}$$

where k_υ and k_ω are suitable gains and $b\,(\phi_2, \psi_2)$ is a function that describes the change in sign of the translational velocity when the state trajectory crosses the singularity. This function can be deduced from the first row of $\mathbf{M}^{-1}$ (11) to be

$$b\,(\phi_2, \psi_2) = -\sin(\phi_2 - \psi_2). \tag{17}$$

The control law (16) with $b\,(\phi_2, \psi_2)$ (17) locally stabilizes the system (10) and is always bounded.

3.1.3 Desired Trajectories for the Epipoles

As main requirement, the desired trajectories must provide a smooth zeroing of the epipoles from their initial values. Fig. 4(a) shows two configurations of robot locations for cases in which $sign\,(e_{23}) \neq sign\,(e_{32})$. From these conditions, the epipoles are naturally reduced to zero as the robot moves directly toward the target. In order to carry out this kind of motion, the locations starting $sign\,(e_{23}) = sign\,(e_{32})$ need to be controlled to the situation of $sign\,(e_{23}) \neq sign\,(e_{32})$. In such case, the control law forces the robot to rotate initially to reach an adequate orientation (Fig. 4(b)). The following trajectories provide the described behavior

$$\begin{aligned} e_{23}^d\,(t) &= \sigma \frac{e_{23}(0)}{2}\left(1 + \cos\left(\frac{\pi}{T}t\right)\right), \quad 0 \leq t \leq T \\ e_{23}^d\,(t) &= 0, \qquad\qquad\qquad\qquad\quad T < t < \infty \\ e_{32}^d\,(t) &= \frac{e_{32}(0)}{2}\left(1 + \cos\left(\frac{\pi}{T}t\right)\right), \quad 0 \leq t \leq T \\ e_{32}^d\,(t) &= 0, \qquad\qquad\qquad\qquad\quad T < t < \infty \end{aligned} \tag{18}$$

where $\sigma = -sign\,(e_{23}(0)e_{32}(0))$ and T is the time to perform the first step of the control strategy. In our approach, as in any image-based scheme, the desired trajectories in the image space play an important role in the resulting Cartesian path. By changing the reference trajectory of the target epipole (related to the translational velocity) is possible to run our approach for car-like robots.

Both previous controllers (15) and (16) can be seen as a commuted control law and their stability is shown later. The control law is able to track the previous references using bounded velocities and its termination condition is set with the time T.

3.2 Second Step.- Depth Correction with Drift Compensation

The commuted controller of the first step is only able to correct orientation and lateral error due to the zero dynamics (9). We have described that a third image allows to define an appropriate control goal to correct the remaining depth. This third image is the initial one and it does not introduce an expensive computational load, given that the corresponding image points are already known and only the 8-point algorithm has to be run. This second step is treated as a regulation problem with integral action to give steady state robustness to the control loop [21], since we have constant desired values (e_{13}, e_{31}).

Let us define error functions $\xi_{12} = e_{12} - e_{13}$ and $\xi_{21} = e_{21} - e_{31}$. We can see from (5) that ξ_{12} does not depend on the rotation and, to avoid coupling problems between inputs, we have chosen its dynamics to work out the translational velocity. Let us define an augmented error system for ξ_{12}, whose dynamics is obtained using (7)

$$\begin{aligned} \dot{\xi}^0_{12} &= e_{12} - e_{13} = \xi_{12}, \\ \dot{\xi}_{12} &= \frac{\alpha_x \sin(\phi_2 - \psi_{12})}{d_{12} \cos^2(\phi_1 - \psi_{12})} v \end{aligned} \tag{19}$$

where the new state ξ^0_{12} corresponds to the integral of the error. The following sliding surface is proposed as the linear combination of the state

$$s = k_0 \xi^0_{12} + \xi_{12} = 0, \tag{20}$$

in such a way that when $s = 0$ we have $\xi_{12} = -k_0 \xi^0_{12}$. By substituting this expression in (19), the reduced order system $\dot{\xi}^0_{12} = -k_0 \xi^0_{12}$ is obtained. It is clear that for any $k_0 > 0$ the reduced dynamic ξ^0_{12} is exponentially stable, and similarly ξ_{12}. We make $\dot{s} = 0$ to find the equivalent control, and then, a switching feedback gain is added to yield

$$v_{dc} = \frac{d_{12_e} \cos^2(\phi_1 - \psi_{12})}{\alpha_{x_e} \sin(\phi_2 - \psi_{12})} (-k_0 \xi_{12} - k_1 sign(s)) \tag{21}$$

where $k_1 > 0$ is a control gain. Notice that $\sin(\phi_2 - \psi_{12})$ is never zero for the situation displayed in Fig. 3(b). This control law achieves robust global stabilization of the system (19) and its termination condition can be given by verifying that $e_{12} - e_{13} \approx 0$.

Although only a straight motion is needed during this second step, orientation control is maintained in order to compensate for the noise or drift that is always present in real situations. We propose to keep the bounded rotational velocity (16) during the second step. However, this velocity depends on e_{23}, which has the problem of short baseline when the target is reached. In order to alleviate this issue, we use a similar approach to the one presented in [16]. An intermediate image is used instead of the target one when the epipolar geometry degenerates. In our case, the last current image of the first step is stored, which corresponds to an image acquired from a location aligned to the target. This intermediate image is denoted by $I_{2_{ar}}(\mathbf{K}, \mathbf{C}_{2_{ar}})$, where the subscript ar stands for "aligned robot". So, the computation of the rotational velocity as the complement of the translational velocity v_{dc} (21) during the second step is carried out from the adequate images as follows

$$\begin{aligned} I_2(\mathbf{K}, \mathbf{C}_2),\ I_3(\mathbf{K}, \mathbf{0}) &\implies \omega_b = -k_\omega sign(e_{23}), \\ I_{2_{ar}}(\mathbf{K}, \mathbf{C}_{2_{ar}}),\ I_2(\mathbf{K}, \mathbf{C}_2) &\implies \omega_b = -k_\omega sign(e_{22_{ar}}). \end{aligned} \tag{22}$$

The second equation is applied when the robot is reaching the target avoiding the problem of short baseline. The condition to switch from the first to the second equation is given by thresholding the value of the epipole e_{23}.

Keeping the control strategy in the same epipolar context has the advantage of providing full control of the position and orientation during the whole task. In previous epipolar approaches, a depth correction stage is carried out by commuting to a feature-based correlation approach with null rotational velocity [7], or by commuting to homography-based control [15]. So, two different approaches are used to solve the visual servoing task in the referred works. In comparison to pure homography-based approaches [5], [6], which depend on the observed plane, our approach is able to correct longitudinal error without an explicit position estimation. Additionally, our control scheme solves the singularity problem by using bounded input velocities while a direct motion to the target is carried out. This problem has been tackled in [7] by avoiding to reach the singularity using a particular motion strategy. The strategy prevents the singularity occurrence, but has the drawback that the robot goes away of the target and then, it performs a backward motion in a second step without orientation control. In [16], one of the control inputs is not computed when crossing the singularity. These aspects show the benefits of the proposed control scheme over previous related approaches.

4 STABILITY ANALYSIS

First, it is worth noting that the servoing task must be accomplished by carrying out the two described steps. In the following, the stability of the tracking control law is analyzed in each step separately. Notice that both steps are independent in the sense that they are applied sequentially. In this analysis, we consider that enough number of image features of the target scene are visible in the camera's field of view during the navigation and that the robot starts in a general location.

Proposition 1. The control law that combines the decoupling-based control (15) by commuting to the bounded control (16) whenever $|\phi_2 - \psi_2| < n\pi + T_h$, where T_h is a suitable threshold and $n \in \mathbb{Z}$, achieves global stabilization of the system (10). Moreover, global stabilization is achieved even with uncertainty in parameters.

Proof Firstly, stabilization of system (10) using controller (15) is proved by showing that the sliding surfaces (12) can be reached in a finite time. Let us consider the natural candidate Lyapunov function for a sliding mode controller,

$$V_{st_1} = V_1 + V_2, \quad V_1 = \tfrac{1}{2}s_c^2, \quad V_2 = \tfrac{1}{2}s_t^2, \tag{23}$$

which accomplishes $V_{st_1}(s_c = 0,\, s_t = 0) = 0$ and $V_{st_1} > 0$ for all $s_c \neq 0$, $s_t \neq 0$, and whose time-derivative is

$$\dot{V}_{st_1} = \dot{V}_1 + \dot{V}_2 = s_c\dot{s}_c + s_t\dot{s}_t. \tag{24}$$

We analyze each term of (24) for the decoupling-based controller (15). Using (10) for the time-derivatives of the sliding surfaces and the estimated parameters α_{x_e} and d_{23_e} in the controller, we have after some simplifications

$$\begin{aligned}
\dot{V}_1 &\leq -\left(\frac{\alpha_x}{\alpha_{x_e}}\left(\kappa_c + \lambda_c\left|s_c\right|\right) - \left|A\right|\right)\left|s_c\right|, \\
\dot{V}_2 &\leq -\left(\frac{\alpha_x d_{23_e}}{\alpha_{x_e} d_{23}}\left(\kappa_t + \lambda_t\left|s_t\right|\right) - \left|B\right|\right)\left|s_t\right|
\end{aligned}$$

where $A = \frac{\alpha_x}{\alpha_{x_e}}\left(\frac{d_{23_e}}{d_{23}} - 1\right)\left(\dot{e}_{32}^d - \kappa_t sign(s_t) - \lambda_t s_t\right)\frac{\cos^2(\psi_2)}{\cos^2(\phi_2 - \psi_2)} + \left(\frac{\alpha_x}{\alpha_{x_e}} - 1\right)\dot{e}_{23}^d$ and $B = \left(\frac{\alpha_x d_{23_e}}{\alpha_{x_e} d_{23}} - 1\right)\dot{e}_{32}^d$ are obtained from $\mathbf{M}\cdot\mathbf{M}_e^{-1}$. Thus, $\dot{V}_1$ and $\dot{V}_2$ are negative definite if and only if the following inequalities are guaranteed for all $s_c \neq 0$, $s_t \neq 0$

$$\begin{aligned}
\kappa_c + \lambda_c\left|s_c\right| &> \frac{\alpha_{x_e}}{\alpha_x}\left|A\right|, \\
\kappa_t + \lambda_t\left|s_t\right| &> \frac{\alpha_{x_e} d_{23}}{\alpha_x d_{23_e}}\left|B\right|.
\end{aligned} \tag{25}$$

Therefore, $\dot{V}_{st_1} < 0$ if and only if both inequalities (25) are fulfilled. On one hand, it is clear that for ideal conditions $d_{23_e} = d_{23}$, $\alpha_{x_e} = \alpha_x$, the right side of both inequalities is zero and therefore, any control gains $\kappa_c > 0$, $\kappa_t > 0$, $\lambda_c > 0$, $\lambda_t > 0$, accomplish the inequalities. On the other hand, when the estimated controller parameters are different to the real ones, the right side of the inequalities become proportional to $\left|\dot{e}_{23}^d\right|$, $\left|\dot{e}_{32}^d\right|$. By using slow references and increasing slightly the gains, global convergence to the sliding surfaces can be achieved regardless of uncertainty in parameters.

Now, let us show the stabilization of system (10) by reaching the surfaces (12) using the controller (16). The same candidate Lyapunov function (23) is used, and for each term of (24) we obtain

$$\begin{aligned}
\dot{V}_1 &\leq -\left(k_\omega\frac{\alpha_x}{\cos^2\left(\phi_2 - \psi_2\right)} - \left|\dot{e}_{23}^d\right| - \left|C\right|\right)\left|s_c\right|, \\
\dot{V}_2 &\leq -\left(k_\upsilon\frac{\alpha_x\left|b\left(\phi_2, \psi_2\right)\right|}{d_{23}\cos^2\left(\psi_2\right)} - \left|\dot{e}_{32}^d\right|\right)\left|s_t\right|.
\end{aligned}$$

where $C = k_\upsilon\frac{\alpha_x|b(\phi_2,\psi_2)|}{d_{23}\cos^2(\phi_2-\psi_2)}sign(s_t)$ and $b\left(\phi_2, \psi_2\right)$ is given in (17). We verify that $\dot{V}_1$ and $\dot{V}_2$ are negative definite if and only if the following inequalities are assured for all $s_c \neq 0$, $s_t \neq 0$

$$\begin{aligned}
k_\omega &> \frac{\cos^2\left(\phi_2 - \psi_2\right)}{\alpha_x}\left(\left|C\right| + \left|\dot{e}_{23}^d\right|\right), \\
k_\upsilon &> \frac{d_{23}\cos^2\left(\psi_2\right)}{\alpha_x\left|b\left(\phi_2, \psi_2\right)\right|}\left|\dot{e}_{32}^d\right|.
\end{aligned} \tag{26}$$

Therefore, $\dot{V}_{st_1} < 0$ if and only if both inequalities (26) are fulfilled. Once again, these inequalities are accomplished by using slow desired trajectories for the epipoles with appropriate gains. Note that these inequalities do not depend on the controller parameters α_{x_e}, d_{23_e} because the bounded controller does not need this information and thus, its robustness is implicit.

Notice that conventional cameras have a constrained field of view and consequently, the commuted control law is able to deal with situations where $|\phi_2 - \psi_2| < \pi/2$. Under such visibility constraint, the fractional terms in any of the previously presented expressions are bounded during the whole navigation task.

The bounded controller (16) is able to locally stabilize the system (10) and its region of attraction grows as long as the control gains k_v and k_ω are higher. Given that the control strategy commutes between two switching controllers according to a rule defined by the threshold T_h (so that each one acts inside of its region of attraction), the commutation between them does not affect the stability of the overall control system.

Once sliding surfaces are reached for any case of SMC law, the system's behavior is independent of matched uncertainties and disturbances. Uncertainties in the system (10) fulfill the matching condition [21]; they belong to the range space of the input vector, and as a result, robustness of the control law is accomplished. ∎

Proposition 2. The translational velocity v_{dc} (21) achieves global stabilization of the system (19) even with uncertainty of parameters, while the rotational velocity (22) achieves lateral drift compensation assuming that Proposition 1 is accomplished.

Proof We prove the stabilization of system (19) by using the controller (21) and showing that the sliding surface (20) can be reached in a finite time. Simultaneously, given the control action (22), the epipoles e_{23} and respectively $e_{22_{ar}}$ are maintained in zero with finite time convergence, keeping the alignment with the target. Let us define the following candidate Lyapunov function

$$V_{st_2} = \frac{1}{2}s^2 + \frac{1}{2}\left(e_{2\star}^2 + e_{\star 2}^2\right)$$

where $\star$ refers to the target $I_3(\mathbf{K}, \mathbf{C}_3)$ or the intermediate image $I_{2_{ar}}(\mathbf{K}, \mathbf{C}_{2_{ar}})$. The time-derivative of this function is

$$\dot{V}_{st_2} = s\dot{s} + e_{2\star}\dot{e}_{2\star} + e_{\star 2}\dot{e}_{\star 2}.$$

The dynamic $\dot{s}$ is obtained from (19) and $\dot{e}_{2\star}$, $\dot{e}_{\star 2}$ are given as follows

$$\begin{aligned} \dot{e}_{2\star} &= \frac{-\alpha_x \sin(\phi_2 - \psi_2)}{d_{2\star}\cos^2(\phi_2 - \psi_2)} v_{dc} + \frac{\alpha_x}{\cos^2(\phi_2 - \psi_2)}\omega_b, \\ \dot{e}_{\star 2} &= \frac{-\alpha_x \sin(\phi_2 - \psi_2)}{d_{2\star}\cos^2(\psi_2)} v_{dc}. \end{aligned} \tag{27}$$

By the assumption that Proposition 1 is accomplished, the robot starts the second step aligned with the target ($x_2 = 0$, $\phi_2 = 0$), which implies $\phi_2 - \psi_2 \approx 0$. Then, we use the small angle approximation $\sin(\phi_2 - \psi_2) \approx 0$, $\cos(\phi_2 - \psi_2) \approx 1$ to obtain

$$\dot{V}_{st_2} = -k_1 \frac{\alpha_x d_{12e}}{\alpha_{x_e} d_{12}} |s| + Ds - k_\omega \alpha_x |e_{2\star}|$$

where $D = \left(1 - \frac{\alpha_x d_{12e}}{\alpha_{x_e} d_{12}}\right) k_0 \xi_{12}$. So, $\dot{V}_{st_2}$ is negative definite if and only if the following inequalities are guaranteed for all $s \neq 0$ and $e_{2\star} \neq 0$

$$\begin{aligned} k_1 &> \frac{\alpha_{x_e} d_{12}}{\alpha_x d_{12e}} |D| \\ k_\omega &> 0 \end{aligned} \tag{28}$$

For ideal conditions, the right side of the first inequality is zero and any value $k_1 > 0$ is enough to reach the sliding surface in finite time. On the contrary, when controller parameters are different to the real ones, the gain k_1 should be increased. Once the sliding mode is reached, the stability of the reduced order system is guaranteed for $k_0 > 0$. Additionally, any disturbance caused by the small angle approximation accomplishes the matching condition and it can be rejected by the SMC input. So, the system (27) is maintained around $e_{2\star} = 0$, $e_{\star 2} = 0$ and the alignment to the target ($\phi_2 = 0$, $x_2 = 0$) is ensured correcting any possible deviation. Finally, the joint action of v_{dc} (21) and ω_b (22) steers the robot in straight motion toward the target in the second step. The stop condition $e_{12} - e_{13} = 0$ guarantees to reach the desired location ($x_2 = 0$, $z_2 = 0$, $\phi_2 = 0$). ∎

Note that the parameters d_{23} and d_{12} are unknown, but according to conditions (25) and (28), they appear as a factor of the translational velocity that can be absorbed by the control gains. However, a good strategy to set the corresponding controller parameters d_{23_e} and d_{12_e} is to over-estimate them, being coherent with the scenario.

Although we are not dealing with a totally uncalibrated case, we have shown that robust global stabilization of the error function can be achieved by setting adequate control gains. Our approach has been developed specifically for mobile robots on the basis of a squared control system unlike some uncalibrated approaches, for instance [18]. Additionally, our approach does not require any additional feedback or initialization information, in contrast to [19].

5 EXPERIMENTAL EVALUATION

5.1 Simulation Results

In this section, some simulations performed in Matlab show that the goal of driving the robot to a desired pose is attained with good performance. The robustness of the approach under parametric uncertainty and noise in the image is reported.

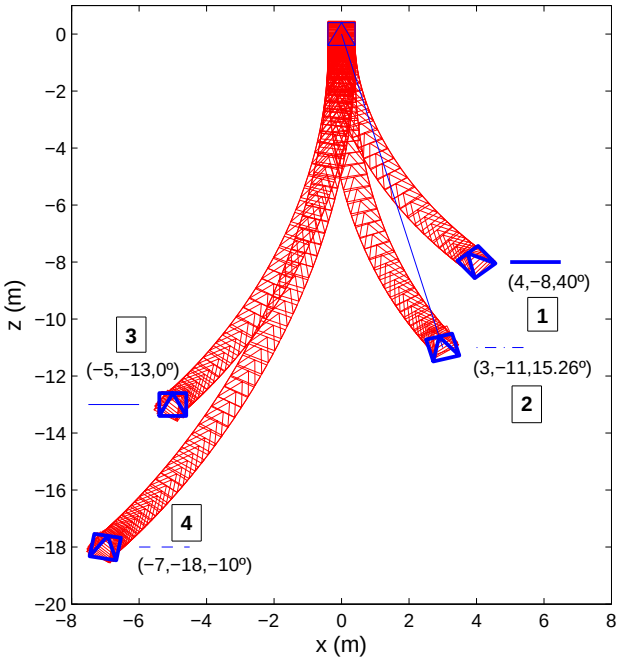

Figure 5: Simulation results: upper view of the robot motion on the $x - z$ plane for different initial locations.

We use virtual images of size 640×480 pixels to compute the epipoles. Along the first simulations we keep fixed all the parameters of the control law. We set $f_e = 6$ mm and $d_{23_e} = 10$ m (the same for d_{12_e}). The simulation time is 20 s ($T = 16$ s corresponding to the first step and the remaining for depth correction) and $T_h = 0.03$ rad. It is enough to set small gains for the bounded controller and unitary gains for the rest of them.

5.1.1 Control through the Singularity

The resultant paths starting from four different locations are shown in Fig. 5. The case 1 is a direct motion toward the target. The case 2 is a situation where the initial pose is singular with $e_{23} = 0$. The line from the initial position to the target shows that the camera axis is aligned with the baseline. At the beginning, the singularity is avoided by the bounded controller, and then, the robot is driven to the target. For the cases 3 and 4 the robot starts with $sign\,(e_{23}) = sign\,(e_{32})$ and e_{23} is controlled to change its sign, which results in the initial rotation.

As an example, the behavior of the state of the robot is presented in Fig. 6(a) for the case 3, where the robot crosses the singularity in the first seconds. This is obtained using the input velocities of Fig. 6(b). The control inputs

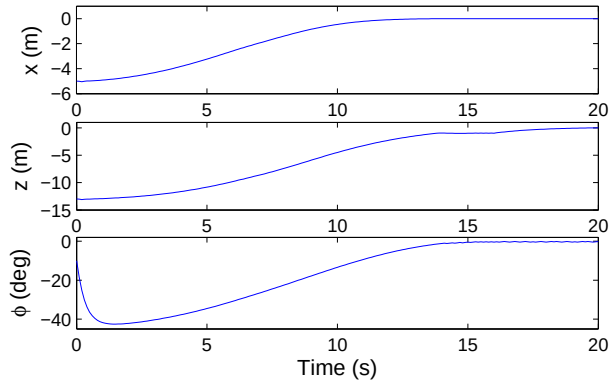

(a) State of the robot.

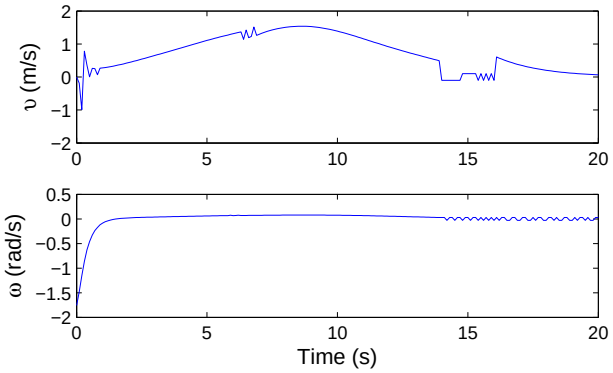

(b) Control inputs.

Figure 6: Simulation results: evolution of the state of the robot and velocities for the case 3 in Fig. 5, where the singularity is crossed in the first seconds.

are maintained bounded even when the robot is aligned with the target around 15 s. The exponential behavior of the translational velocity from 16 s to 20 s corrects the remaining depth error.

5.1.2 Robustness under Parametric Uncertainty and Noise

The control law has shown robustness under error in the parameters d_{23}, d_{12} with respect to the introduced in the controller d_{23_e}, d_{12_e}. Up to now, all the control law parameters have been maintained as described before. Notice that for the four previous paths, the distance (d_{23} in meters) between cameras is different for each initial pose, and even so the target is reached.

Regarding to camera parameters uncertainty, we analyze the effect of changing the focal length (f) in the computation of epipoles while keeping f_e constant in the controller. The initial pose is (2,-7,30^o) for all the simulation runs, however, the obtained behavior is recurrent for any initial pose. Figure 7 presents the final pose and mean squared tracking error for a range of focal lengths. The robot always reaches the target with good precision and the tracking error is maintained in a low value. The last plot in Fig. 7 shows the final pose for different values of the x-coordinate of the principal point.

Figure 8(a) shows the performance of the approach under image noise for the initial pose (-6,-16,-10^o). The simulation time is set to 40 s and the noise added to the image points has a standard deviation of 0.5 pixels. It is clear the presence of this noise in the motion of the image points in Fig. 8(b). In Fig. 8(c) we can see the exponential behavior of the depth after $T = 32$ s, which reaches zero by using feedback from e_{12}. We can notice in Fig. 8(d) that the epipoles e_{23} and e_{32} become unstable before the end. However, after 32 s the controller uses e_{12} to compute the translational velocity by regulating e_{12} to a constant value as shown in Fig. 8(e). We can see that e_{21} is more sensitive because also depends on the rotational velocity, but it is not used in the controller. The corresponding input velocities obtained by the control algorithm are shown in Fig. 8(f). Notice that none of both velocities have the problem of short baseline at the end of the motion, since they are computed from stable measurements (e_{12} and $e_{22_{ar}}$, respectively).

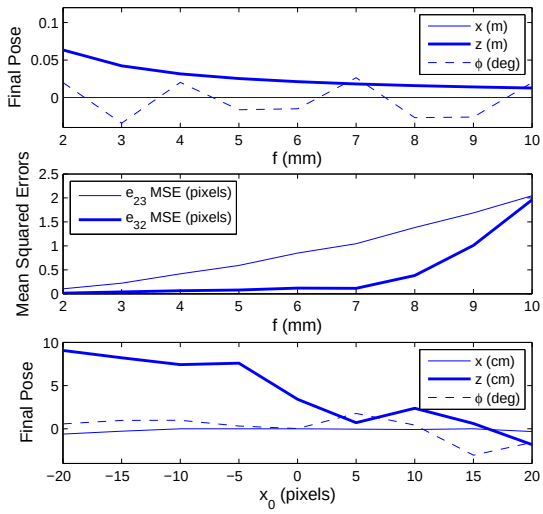

Figure 7: Simulations with different values of focal length (f) and principal point (x_0) showing robustness against parametric uncertainty.

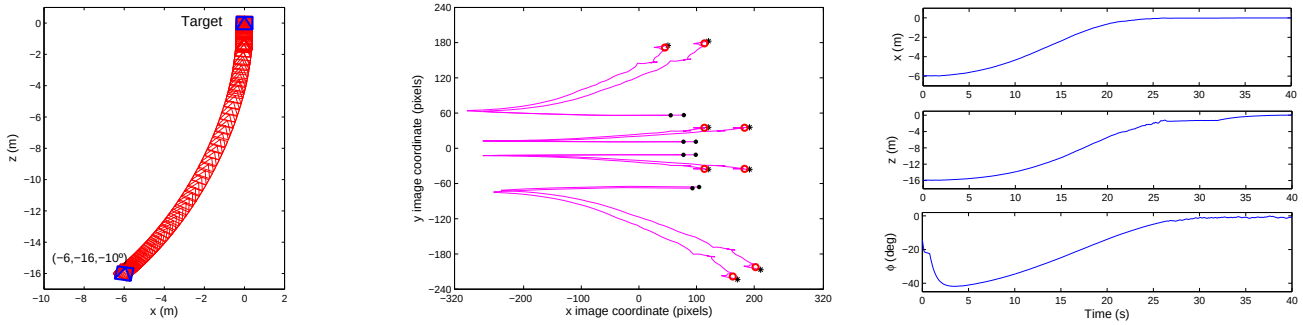

(a) Path on the $x-z$ plane. (b) Image points motion ('o'-tar, '·'-ini). (c) State of the robot.

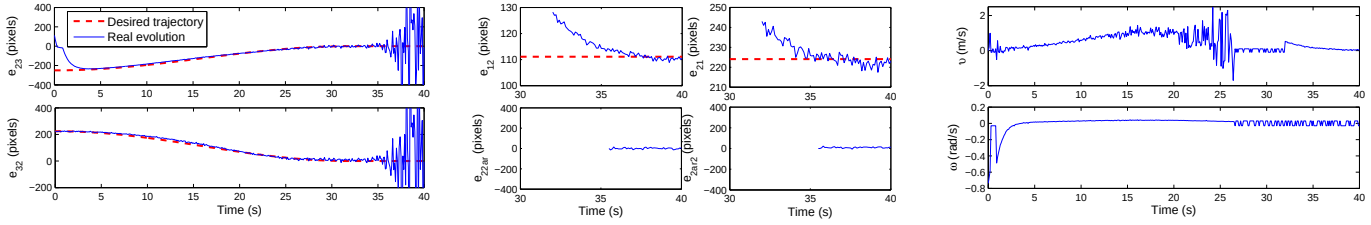

(d) Epipoles e_{23}, e_{32}. (e) Epipoles e_{12}, e_{21}, $e_{22_{ar}}$, $e_{2_{ar}2}$. (f) Control inputs.

Figure 8: Simulation results. (a) Robot trajectory. (b) Motion of the points in the image. (c) State variables of the robot during the motion. (d) Epipoles e_{23} and e_{32} used to compute decoupled velocities (15) until 26 s and the bounded velocities (16) until 32 s. The same rotational velocity from e_{23} is maintained until 35.5 s. As e_{23} turns out unstable, from 35.5 s to 40 s $e_{22_{ar}}$ (e) is used to compute the rotational velocity according to (22). The translational velocity from 32 s to 40 s is computed from e_{12} (e) using (21). In (f), the resulting velocities υ and ω during the global trajectory are shown. Although e_{21} and $e_{2_{ar}2}$ in (e) are not used, they are shown to illustrate their proper convergence.

5.2 Real-world Experiments

The proposed control law has been tested in real conditions using the robot Pioneer P3-DX of Fig. 1(b) with a low cost conventional camera. The images are acquired at size 640×480 pixels. In order to facilitate the image processing, the scene observed has been set up with two planes consisting on squared patterns, from which the corners of the squares are extracted and matched to estimate the epipolar geometry. The acquired image data is processed using the OpenCV library. During the navigation, the system tracks the image points using a Lucas-Kanade pyramidal algorithm. The corresponding points are the entries of the 8-point algorithm as implemented in OpenCV.

The control law parameters have been set to $d_{23_e} = d_{12_e} = 5$ m and $f_e = 9$ mm, and the image center as the principal point without performing specific calibration. Figures 9(a)-(b) present the evolution of the state given by the robot odometry, from the initial location (-0.3 m,-1.3 m,0^o) for one of the experimental runs. The final position error is less than 5 cm and the orientation error is practically negligible. The time T for the execution of the first step, alignment with the target, is set to 21 s. We can see in Fig. 9(c) how the bounded SMC law is applied around 16 s due to the occurrence of the singularity. After 21 s the feedback for depth correction is provided from the error of e_{12}. The behavior of those epipoles involved in the control law is shown in Fig. 9(d). The termination condition of the task is given when the difference $e_{12} - e_{13}$ is below a threshold. Figure 10 shows sequences of some images taken by the robot camera and an external video camera.

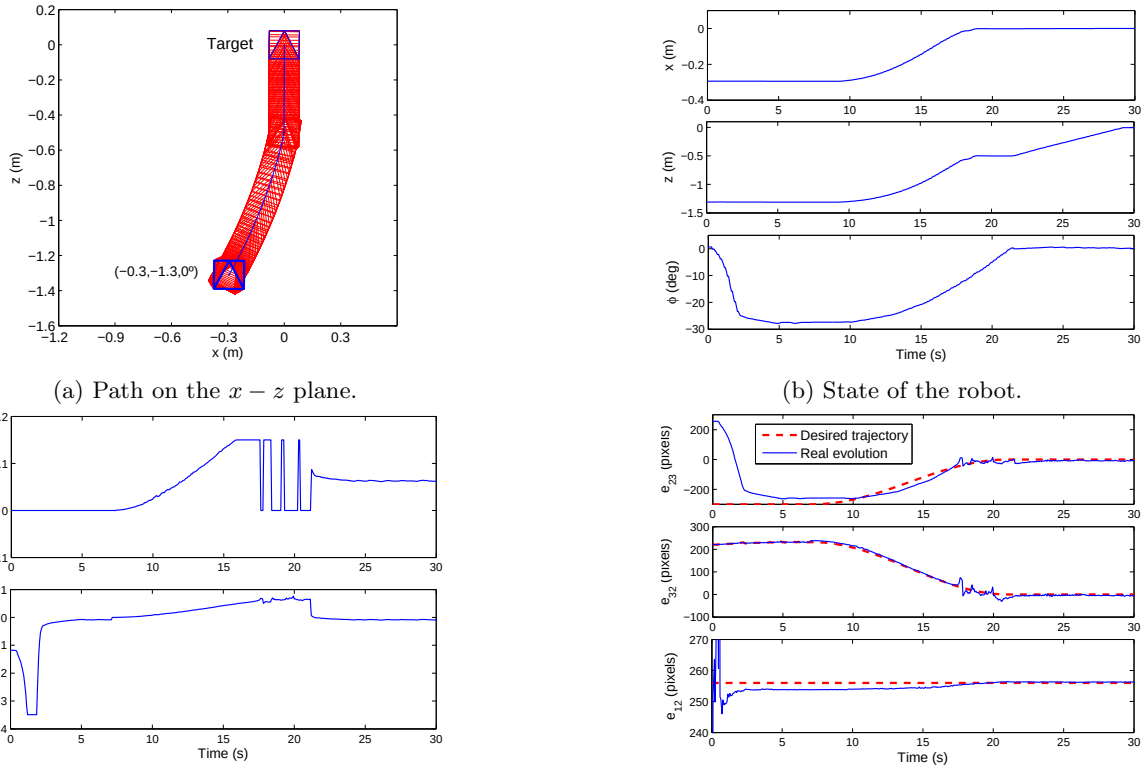

(a) Path on the $x - z$ plane.

(b) State of the robot.

(c) Control inputs.

(d) Evolution of the epipoles.

Figure 9: Real experiment with target location (0,0,0^o). The data presented in (a)-(b) corresponds to the robot odometry.

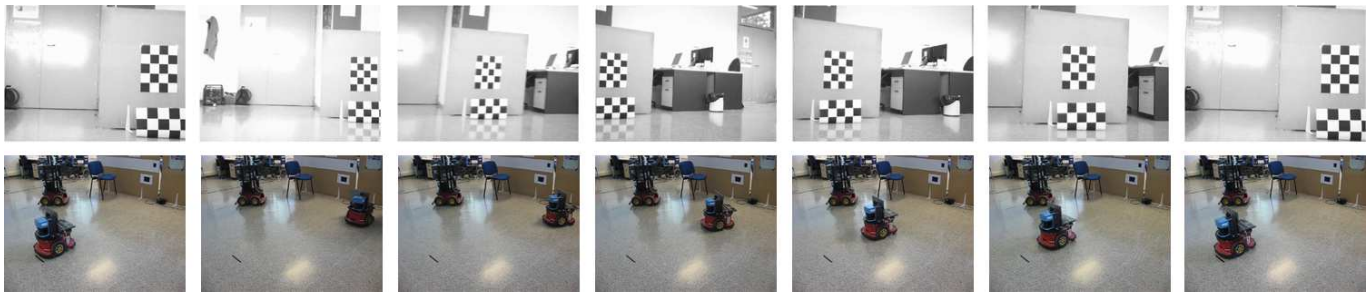

Figure 10: Sequence of some images taken from the robot camera (1st row) and from an external camera (2nd row) during the real experiment. The first is the target image, the second is the initial and the last is the image at the end of the motion. The robot behind is not involved in the experiment.

The non-ideal behavior of the tracking for e_{23} is due to the hardware constraints, given that the closed loop frequency is limited in the robots at our disposal. Nevertheless, simulations and real-world experiments show that a closed loop frequency around 10 Hz is enough to obtain system's behavior with small chattering effect. Chattering is a phenomenon presented in SMC systems that generates an oscillation within a neighborhood of the switching surface such that $\mathbf{s} = \mathbf{0}$

is not satisfied as expected ideally [22]. In our results, given the frequency achieved and because of the low-pass filtering effect of the robotic mechanical system, the state of the robot has a smooth behavior. The resultant navigation in this experiment is shown in a video together with the view of the on-board camera. This shows the validity of our proposal and its satisfactory performance with the hardware used. As long as the closed loop frequency could be higher the results could be improved.

6 CONCLUSIONS

In this paper, a robust control law based on sliding mode theory has been presented in order to perform image-based visual servoing of mobile robots. The approach is valid for differential-drive wheeled robots moving on a plane and carrying a conventional camera onboard. The generic control law has been designed on the basis of kinematics control by exploiting the pairwise epipolar geometries of three views.

The contribution of the paper is a novel control law that performs orientation, lateral error and depth correction without needing to change to any approach other than epipolar-based control. The control scheme deals with singularities induced by the epipolar geometry maintaining always bounded inputs, which allows the robot to carry out a direct motion toward the target. Additionally, it is a robust approach that does not need a precise camera calibration.

On one hand, the approach can be used provided that there are enough point features to estimate the epipolar geometry between the views. On the other hand, the SMC requires an adequate closed loop frequency, which can be achieved in typical experimental hardware as shown in our real-world experiments.

References

[1] S. Hutchinson, G. D. Hager, and P. I. Corke. A tutorial on visual servo control. *IEEE Transactions on Robotics and Automation*, 12(5):651–670, 1996.

[2] G. N. DeSouza and A. C. Kak. Vision for mobile robot navigation: A survey. *IEEE Trans. on Patt. Analysis and Machine Intelligence*, 24(2):237–267, 2002.

[3] Y. Masutani, M. Mikawa, N. Maru, and F. Miyazaki. Visual servoing for non-holonomic mobile robots. In *IEEE/RSJ International Conference on Intelligent Robots and Systems*, pages 1133–1140, 1994.

[4] D. Tsakiris, P. Rives, and C. Samson. Extending visual servoing techniques to nonholonomic mobile robots. In *Lecture Notes in Control and Informations Systems. The Confluence of Vision and Control*, volume 237, pages 106–117. Spriger-Verlag, 1998.

[5] Y. Fang, W. E. Dixon, D. M. Dawson, and P. Chawda. Homography-based visual servo regulation of mobile robots. *IEEE Transactions on Systems, Man, and Cybernetics - Part B: Cybernetics*, 35(5):1041–1050, 2005.

[6] G. López-Nicolás, C. Sagüés, and J.J. Guerrero. Homography-based visual control of nonholonomic vehicles. In *IEEE International Conference on Robotics and Automation*, pages 1703–1708, 2007.

[7] G. L. Mariottini, G. Oriolo, and D. Prattichizzo. Image-based visual servoing for nonholonomic mobile robots using epipolar geometry. *IEEE Transactions on Robotics*, 23(1):87–100, 2007.

[8] H. M. Becerra, G. López-Nicolás, and C. Sagüés. Omnidirectional visual control of mobile robots based on the 1D trifocal tensor. *Robotics and Autonomous Systems*, 58(6):796–808, 2010.

[9] F. Chaumette and S. Hutchinson. Visual servo control Part I: Basic approaches. *IEEE Robotics and Automation Magazine*, 13(14):82–90, 2006.

[10] F. Chaumette. Potential problems of stability and convergence in image-based and position-based visual servoing. In *Lecture Notes in Control and Informations Systems. The Confluence of Vision and Control*, volume 237, pages 66–78. Spriger-Verlag, 1998.

[11] N. Andreff, B. Espiau, and R. Horaud. Visual servoing from lines. *The International Journal of Robotics Research*, 21(8):679–699, 2002.

[12] R. Hartley and A. Zisserman. *Multiple View Geometry in Computer Vision*. Cambridge University Press, Cambridge, second edition, 2004.

[13] R. Basri, E. Rivlin, and I. Shimshoni. Visual homing: Surfing on the epipoles. *International Journal of Computer Vision*, 33(2):117–137, 1999.

[14] P. Rives. Visual servoing based on epipolar geometry. In *IEEE/RSJ International Conference on Intelligent Robots and Systems*, pages 602–607, 2000.

[15] G. López-Nicolás, J.J. Guerrero, and C. Sagüés. Visual control of vehicles using two-view geometry. *Mechatronics*, 20(2):315–325, 2010.

[16] G. López-Nicolás, C. Sagüés, J.J. Guerrero, D. Kragic, and P. Jensfelt. Switching visual control based on epipoles for mobile robots. *Robotics and Autonomous Systems*, 56(7):592–603, 2008.

[17] J. Courbon, Y. Mezouar, and P. Martinet. Autonomous navigation of vehicles from a visual memory using a generic camera model. *IEEE Trans. on Intelligent Transportation Systems*, 10(3):392–402, 2009.

[18] E. Malis. Visual servoing invariant to changes in camera-intrinsic parameters. *IEEE Transactions on Robotics and Automation*, 20(1):72–81, 2004.

[19] H. Wang, Y. H. Liu, and D. Zhou. Adaptive visual servoing using point and line features with an uncalibrated eye-in-hand camera. *IEEE Transactions on Robotics*, 24(4):843–857, 2008.

[20] H. M. Becerra and C. Sagues. A sliding mode control law for epipolar visual servoing of differential-drive robots. In *IEEE/RSJ International Conference on Intelligent Robots and Systems*, pages 3058–3063, 2008.

[21] H. K. Khalil. *Nonlinear Systems*. Prentice Hall, third edition, 2001.

[22] V. Utkin, J. Guldner, and J. Shi. *Sliding Mode Control in Electromechanical Systems*. CRC Press, Boca Raton, 1999.

[23] R. M. Hirschorn. Output tracking through singularities. In *IEEE Conference on Decision and Control*, pages 3843–3848, 2002.